In Situ Characterization of Dynamic Morphological and Phase Changes of Selenium-doped Germanium Using a Single Particle Cell and Synchrotron Transmission X-ray Microscopy

Dr. Tianyi Li[a], Dr. Xinwei Zhou[a,b], Dr. Yi Cui[a], Melissa L. Meyerson[c], Jason A. Weeks[c], Prof. C. Buddie Mullins[c], Dr. Vincent De Andrade[d], Dr. Francesco De Carlo[d], Dr. Yuzi Liu[b], and Prof. Likun Zhu[a*]

[a]Department of Mechanical and Energy Engineering, Indiana University Purdue University Indianapolis, Indianapolis, IN 46202

[b]Center of Nanoscale Materials, Argonne National Laboratory, Argonne, IL 60439

[c]Departments of Chemical Engineering and Chemistry, University of Texas at Austin, Austin, TX 78712

[d]Advanced Photon Source, Argonne National Laboratory, Argonne, IL 60439

[*]Corresponding Author:

Likun Zhu

Department of Mechanical and Energy Engineering

Indiana University Purdue University Indianapolis

723 W. Michigan Street, Room SL 260 L

Indianapolis, IN 46202

Phone: 1-317-274-4887

Fax: 1-317-274-9744

Email: likzhu@iupui.edu

This is the author's manuscript of the article published in final edited form as:

Li, T., Zhou, X., Cui, Y., Meyerson, M. L., Weeks, J. A., Buddie Mullins, C., De Andrade, V., De Carlo, F., Liu, Y., & Zhu, L. (2021). In-Situ Characterization of Dynamic Morphological and Phase Changes of Selenium-doped Germanium Using a Single Particle Cell and Synchrotron Transmission X-ray Microscopy. ChemSusChem, 14(5), 1370–1376. https://doi.org/10.1002/cssc.202002776

Table of Content

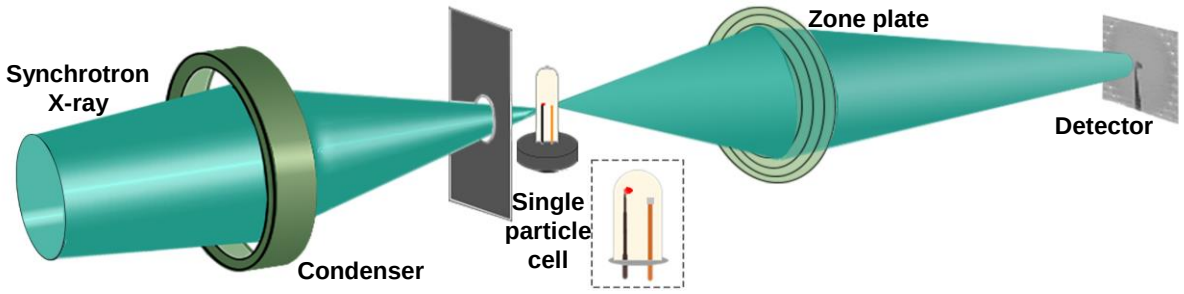

In situ single particle battery: An in situ single particle cell is developed to characterize the dynamic electrochemical processes of lithium ion battery electrode materials at a single particle level using synchrotron transmission X-ray microscopy.

Abstract

The dynamic information of lithium ion battery active materials obtained from coin cell-based in situ characterizations might not represent the properties of the active material itself because many other factors in the cell could have impacts on the cell performance. To address this problem, a single particle cell was developed to perform the in situ characterization without the interference of inactive materials in the battery electrode as well as the X-ray-induced damage. In this study, the dynamic morphological and phase changes of selenium-doped germanium ($Ge_{0.9}Se_{0.1}$) at the single particle level were investigated via synchrotron-based in situ transmission X-ray microscopy. The results demonstrate the good reversibility of $Ge_{0.9}Se_{0.1}$ at high cycling rate that helps understand its good cycling performance and rate capability. This in situ and operando technique based on a single particle battery cell provides an approach to understanding the dynamic electrochemical processes of battery materials during charging and discharging at the particle level.

Keywords: In situ characterization, lithium ion battery, selenium-doped germanium, single particle cell, synchrotron transmission X-ray microscopy

Introduction

Lithium ion batteries (LIBs) have emerged as a leading energy storage technology for electric vehicles and electronics. The continuing need for higher energy density and better rate capability requires a fundamental understanding of the dynamic electrochemical processes in battery electrodes at multiple length scales [1]. The electrochemical processes of LIB electrode materials are often accompanied by structural, morphological, and chemical evolution during battery cycling. Understanding these dynamic processes during charging and discharging requires advanced operando measurement to investigate structural and chemical information at high spatial resolution. Recently, X-ray computed tomography with nanometers resolution has been used for tracking the degradation in LIBs and has provided valuable microstructural images in three-dimensions (3D). However, the traditional in situ coin cell with Kapton windows do not have uniform stack pressure and electrical conductance along the punched holes [2] which may cause abnormal reactions for the sample area underneath the window during operando transmission X-ray microscopy (TXM) [3] and X-ray diffraction (XRD) [4] measurements. This inhomogeneity can cause the active materials in contact with the Kapton window to have different electrochemical kinetics compared to the others. To address this problem, a multipurpose X-ray (AMPIX) cell has been developed recently at the Argonne National Laboratory to provide a more reliable electrochemical setup due to its homogeneous stack pressure and rigid electrically conductive windows [5]. However, these setups have rotating limitations that make tomography experiments difficult. The coin cell also suffers from X-ray-induced damage to the polymer binder [6], which can disconnect the active material particles from the current collector and make them inactive. In addition, the coin cell involves interactions among active material particles [3], which can affect the dynamic information.

To develop a working cell compatible with tomography is challenging because the cell must function normally as a working battery without blocking the X-ray beam over 180 degrees of rotation. Wang et al. synthesized carbon-coated tin particles on carbon paper via a chemical vapor deposition method [7]. The electrode was modified and fabricated into a Kapton capillary cell for X-ray nanotomography analysis. Regardless of what counter electrode they employed, whether lithium or sodium, the interaction between different active material particles on the same electrode was inevitable. Lim et al. employed a carbon wire electrode coated by germanium (Ge) microparticle slurry for operando transmission X-ray microscopy and in situ computed tomography. In this experiment, some of the active material particles were active while a few of them were inactive due to the intensive X-ray exposure [8]. The low stiffness of the carbon wire electrode induced slight movement and rotation during the entire measurement, which makes reconstruction and analysis difficult. Zhou et al. developed an in situ focused ion beam-scanning electron microscopy (FIB-SEM) technique and employed it to investigate the microstructural evolution of a variety of high capacity battery materials [9]. However, the irreversible damage to the material due to the focused ion beam polishing is permanent and unavoidable. In addition, an ionic liquid electrolyte has to be used in the vacuum environment of the FIB-SEM chamber, which is different from the organic solvent-based electrolyte used in commercial LIBs. There exists a need for techniques that can investigate the properties of electrode materials in a manner that can avoid interference from the other factors. The electrodes of LIBs include active material particles, carbon additives, polymer binders, and current collectors. These complicated architectures and components of the conventional electrodes lead to interactions between each component and variations in both particle size and shape distributions. It is difficult to extract the

dynamic properties of the active material itself. Tsai et al. recently reported the three-dimensional microstructural evolution of $LiNi_{1/3}Mn_{1/3}Co_{1/3}O_2$ (NMC) and $LiNi_{0.8}Co_{0.15}Al_{0.05}O_2$ (NCA) cathode materials in a single particle cell via ex-situ synchrotron TXM nanotomography [1]. They used similarly sized spherical particles and performed cycling experiments at C/3 in an argon-filled glovebox to each specific voltage and ex-situ tomography images were collected. Although the particles have similar sizes, there are variances including shapes, manufacturing differences, and chemical distributions inside each individual object. These diversities have potential influences on the phenomena observed.

To address these challenges, we developed a single particle battery for in situ transmission X-ray microscopy with energy scan and X-ray computed tomography measurements for the pristine, lithiated, and delithiated states. In this study, selenium-doped germanium ($Ge_{0.9}Se_{0.1}$) was tested using the developed in situ single particle battery. Klavetter et al. had demonstrated by doping a small portion of selenium into germanium, the network formed during cycling has the ability to alleviate strain and enhance lithium diffusion, and therefore, increase its electrochemical performance [10]. This phenomenon was further proven by operando XRD, TXM, and X-ray absorption spectroscopy (XAS) as reported in ref [8]. In this study, we selected micron-sized $Ge_{0.9}Se_{0.1}$ to ensure the practical relevance of the results to the traditional coin cell. The single particle cell was galvanostatically cycled between 0.01 and 1.5 V. The operando TXM was employed periodically to monitor the morphological changes under operating conditions while in situ transmission X-ray microscopy with energy scan and computed tomography was conducted at each critical state. Using these combined techniques, the dynamic morphological changes,

volumetric expansion in 3D, and chemical compositions are characterized at the single particle level for the first time.

Results and Discussion

To understand the dynamic morphological and chemical changes of the active materials without the interference of carbon and binder additives, we have developed a single particle battery cell for operando TXM and in situ computed tomography. This binder-free in situ single particle cell eliminates discrepancies caused by particles overlapping in the in-situ coin cell during TXM and the impact of X-ray-induced damage to the binder [6], which provides chemical and morphological information in 3D. The $Ge_{0.9}Se_{0.1}$ single particle cell was cycled at 1 C rate.

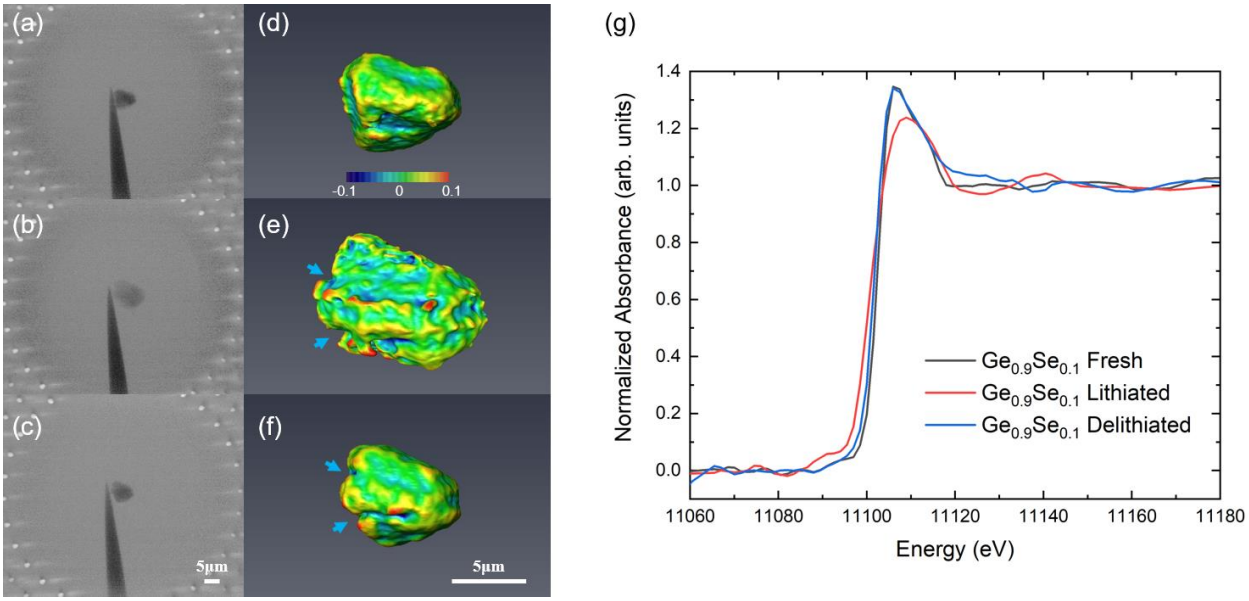

Figure 1. The TXM and corresponding 3D morphological evolutions of a single $Ge_{0.9}Se_{0.1}$ particle cell at the (a,d) pristine, (b,e) lithiated, and (c,f) delithiated states. (g) XANES spectra generated via transmission X-ray microscopy images.

Figure 1 displays the 2D TXM images (a-c) and the corresponding 3D mean surface curvature view (d-f) of a $Ge_{0.9}Se_{0.1}$ particle attached to a tungsten probe captured at 11200 eV while the tungsten probe was set to be invisible during visualization. The volume expansion of the $Ge_{0.9}Se_{0.1}$ particle is about 293% after lithiation, which is close to the theoretical volume expansion of Ge [9b]. After delithiation, the particle recovered back to its original shape and the volume is slightly larger (4%) than its pristine state. As pointed to by the arrows in Figure 1e and f, there are two cracks generated during the lithiation process and retained during the delithiation process. These two cracks were initiated from the defects caused by the focused ion beam during the carbon deposition. Figure 1g shows the X-ray absorption near edge structure (XANES) spectra of the $Ge_{0.9}Se_{0.1}$ particle at pristine, lithiated, and delithiated states. After lithiation, the white line shifted to higher energy, which indicates the formation of Li_xGe alloy. The XANES spectra also show that the chemical composition after delithiation has the same white line position and almost identical shape compared with its pristine state. The XANES results and the volume change of the $Ge_{0.9}Se_{0.1}$ particle demonstrate that almost all the lithium ions are reversible during the lithiation and delithiation processes at a 1 C rate in the $Ge_{0.9}Se_{0.1}$ single particle cell. The XANES results of the single particle cell are different from previous studies via operando XAS or TXM for coin cells in which the white line positions of the pristine and delithiated states are slightly different. The in situ coin cells suffer from the interactions between complex architectures of the electrode, volume expansion, and the formation of cracks that might cause delamination of the active materials from the current collector, therefore limiting the intercalation and extraction of lithium ions.

The dynamic morphological change of the $Ge_{0.9}Se_{0.1}$ particle is shown in the video in the supporting information. By selecting the contour line of its pristine state as the area of interest (Figure 2a), the optical density (OD) of the single $Ge_{0.9}Se_{0.1}$ particle changed from 1 at its pristine state to 0.4 after lithiation and recovered back to 1 when delithiation was completed as shown in Figure 2b. Comparing with the OD results in ref [8], the in situ single particle cell exhibits an OD value close to 1 at its pristine state, and a minimum OD value of 0.4 after lithiation was completed. The lower OD value compared to ref [8] indicates that a more completed reaction was acquired. The OD value of $Ge_{0.9}Se_{0.1}$ was able to recover back to 1 further illustrating its good reversibility, which is consistent with the TXM and XANES results shown in Figure 1. The single particle-based OD analysis is linear for both lithiation and delithiation processes, which differs from the traditional coin cell result presented in ref [8]. These differences may be due to the inhomogeneous stack pressure along the X-ray pathway through the punched holes for the traditional modified coin cell as well as the interactions between individual active material particles in the electrode. Previous studies have revealed the mechanisms of the outstanding cycling performance of $Ge_{0.9}Se_{0.1}$ material by coin cell-based characterizations, such as operando TXM, XRD and XAS [8, 10]. The selenium doping not only has the ability to accelerate lithium diffusion and suppress the formation of $Li_{15}Ge_4$ as reported in ref [8] but also preserves the morphological and volumetric characteristics. Based on the line profile analysis shown in Figure 2d, an obvious intensity change was observed during lithiation when the time frame reaches 20 min. The intensity gradient becomes smaller between the particle and the background as well as the tungsten probe due to the propagation of lithium ions from the surface to the core of the $Ge_{0.9}Se_{0.1}$ particle. At the end of lithiation, the boundary of the particle expands 120 pixels and the line profile becomes flat with an intensity value close to the

background. The line profile was recovered back to its original state after delithiation, which demonstrates its good reversibility.

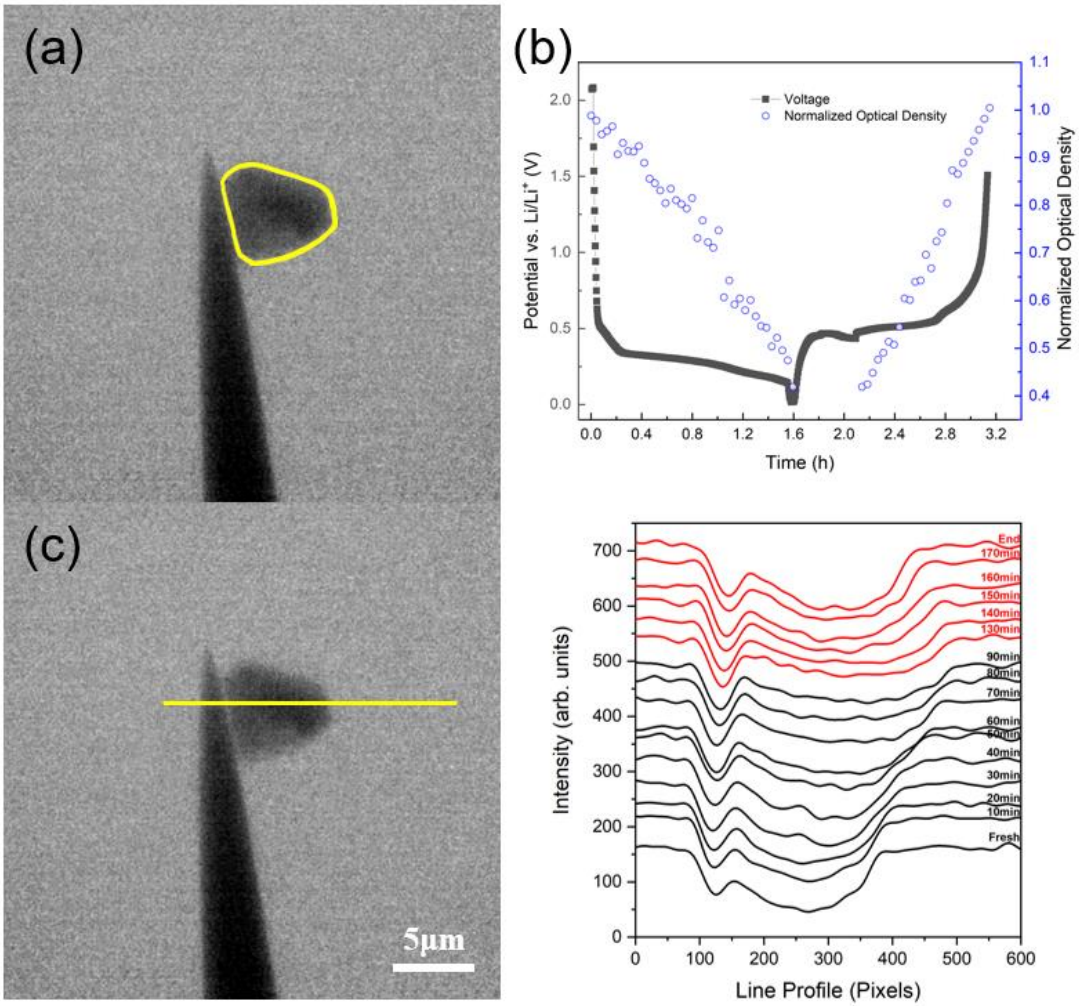

Figure 2. (a, c) Area of interest as highlighted in yellow of the single $Ge_{0.9}Se_{0.1}$ particle cell and (b, d) the corresponding optical density and line profile analysis results at the selected time frame. The cell was under relaxation with no current between 1.6-2.1 h during imaging for in situ tomography and XANES.

To compare with the single particle cell, an in situ $Ge_{0.9}Se_{0.1}$ coin cell with Kapton window was fabricated and cycled at a 1 C rate and in situ XANES experiments were conducted for the pristine, lithiated, and delithiated states. As shown in Figure 3a, the voltage profile shows the reaction plateaus of Ge in both the discharging and charging processes. However, the shape of the XANES spectra at lithiated and delithiated states shown in Figure 3b is mostly identical to its pristine state, which indicates limited lithium ions were consumed by the active material particles during the high current cycling for the area where images were captured. To investigate the morphological changes of $Ge_{0.9}Se_{0.1}$ particles, image registration and subtraction were performed by using three images from the pristine, the end of lithiation, and the end of delithiation as shown in Figure 3c-e. Figure 3f and g show the differences between these images. Since there are almost no black areas in Figure 3f and g, it indicates that most of the $Ge_{0.9}Se_{0.1}$ particles in the image did not have volume change during the 1 C cycling process, which is consistent with the XANES results shown in Figure 3b. Similar phenomena were previously observed in ref [3, 11], which is due to the nonuniform stack pressure and current inhomogeneities caused by the punched holes. The area of the punched holes is 0.0003 cm^2 compared to the entire electrode of 1 cm^2, which represents only 0.03% of the area. Therefore, incomplete reactions along the X-ray pathway may not affect the entire performance significantly. Hence, the complex architecture of the electrode with multiple variables influences the performance of the active material itself. The proposed single particle cell isolates uncertainties caused by additives in the traditional electrode, which provides more accurate and reliable experiment results.

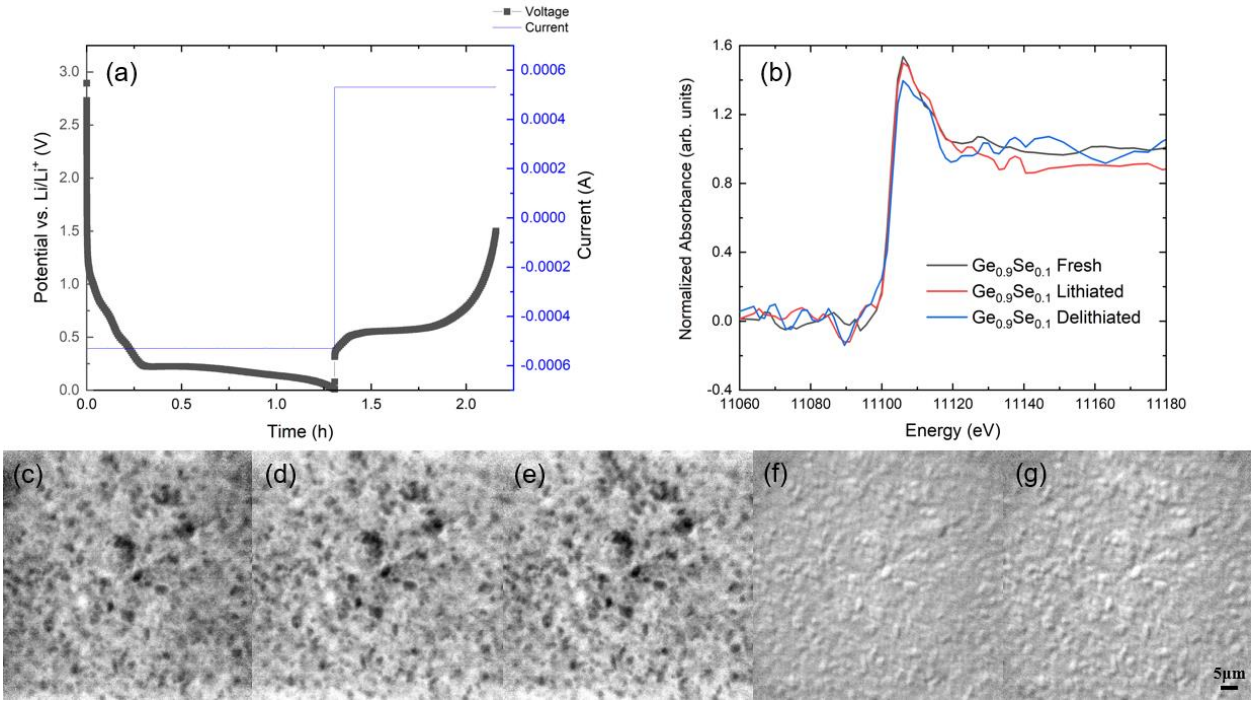

Figure 3. (a) Potential plots of a $Ge_{0.9}Se_{0.1}$ electrode cycled at a 1 C rate in the in situ coin cell and (b) the corresponding transmission X-ray microscopy-based germanium XANES spectra. (c) TXM image of the pristine $Ge_{0.9}Se_{0.1}$ electrode. (d) TXM image of the lithiated $Ge_{0.9}Se_{0.1}$ electrode. (e) TXM image of the delithiated $Ge_{0.9}Se_{0.1}$ electrode. (f) differences between (c) and (d) by image subtraction. (g) differences between (d) and (e) by image subtraction.

To validate the coin cell performance at 1 C, a smaller current was employed for the in situ coin cell for comparison as well. Images were captured periodically to monitor the chemical and morphological changes for the $Ge_{0.9}Se_{0.1}$ electrode at 0.1 C. The radiographs were recorded at each 60 min interval during their first cycle. There are some missing data, which is due to the unexpected beam outage at the APS during the battery cycling process. The $Ge_{0.9}Se_{0.1}$ XANES spectra shown in Figure 4 were calculated and normalized based on the entire electrode

visualized in each TXM image sequence. The white line of the Ge spectrum is sharp at the beginning and becomes broader as lithiation proceeds (after 7 hours) for the $Ge_{0.9}Se_{0.1}$ electrode. The broadening of the peak shape means that the electrons in Ge are less confined, which is due to either the amorphization process or crystal lattice increase [12]. The shape transformation of Ge spectra without a distinct peak at 11113 eV indicates the formation of amorphous Li_xGe phases. At the end of delithiation, the Ge spectrum was partially recovered but it does not exhibit the same shape as its pristine state, which demonstrates the formation of amorphous Ge after delithiation and residual Li_xGe phases due to the impact of X-rays on the carbon binder matrix as reported in ref [4a]. These observations were previously reported in references [4a, 8] via operando XAS measurements and are now validated through the TXM experiments reported here. The current rate applied to the in situ coin cells plays an essential role during the operando experiment. Comparing the XANES spectra between Figure 3 and Figure 4, the high current rate applied upon cycling with weak stack pressure along the X-ray route may lead to a large resistance and lagged electrochemical reaction, and therefore, influence the reaction phenomenon observed. The slow current rate diminished the current inhomogeneity which alleviates the impact of resistance and reinforces a more complete reaction. Figure 4 exhibits similar results compared with the single particle $Ge_{0.9}Se_{0.1}$ anode material in Figure 1g during lithiation with differences in the delithiation process, which is mainly caused by the complex architecture and the incomplete delithiation reaction in the coin cells. The TXM images from the pristine, lithiated, and delithiated states are shown in Figure 4 b-d. The black spots displayed in Figure 4e demonstrate the differences between its pristine and lithiated states. Most of the active material particles have been lithiated during the discharging process. As shown in Figure 4f, only a few active material particles were delithiated and partially recovered. Although the coin cell may

represent a real-world battery, it exhibits different phenomena compared with the single particle cell. Nevertheless, the dynamic electrochemical processes of the active materials in the coin cell was affected by the complicated architecture and components of the conventional electrodes. The single particle cell can reveal the dynamic properties of the material and benefit the understanding of the active material itself.

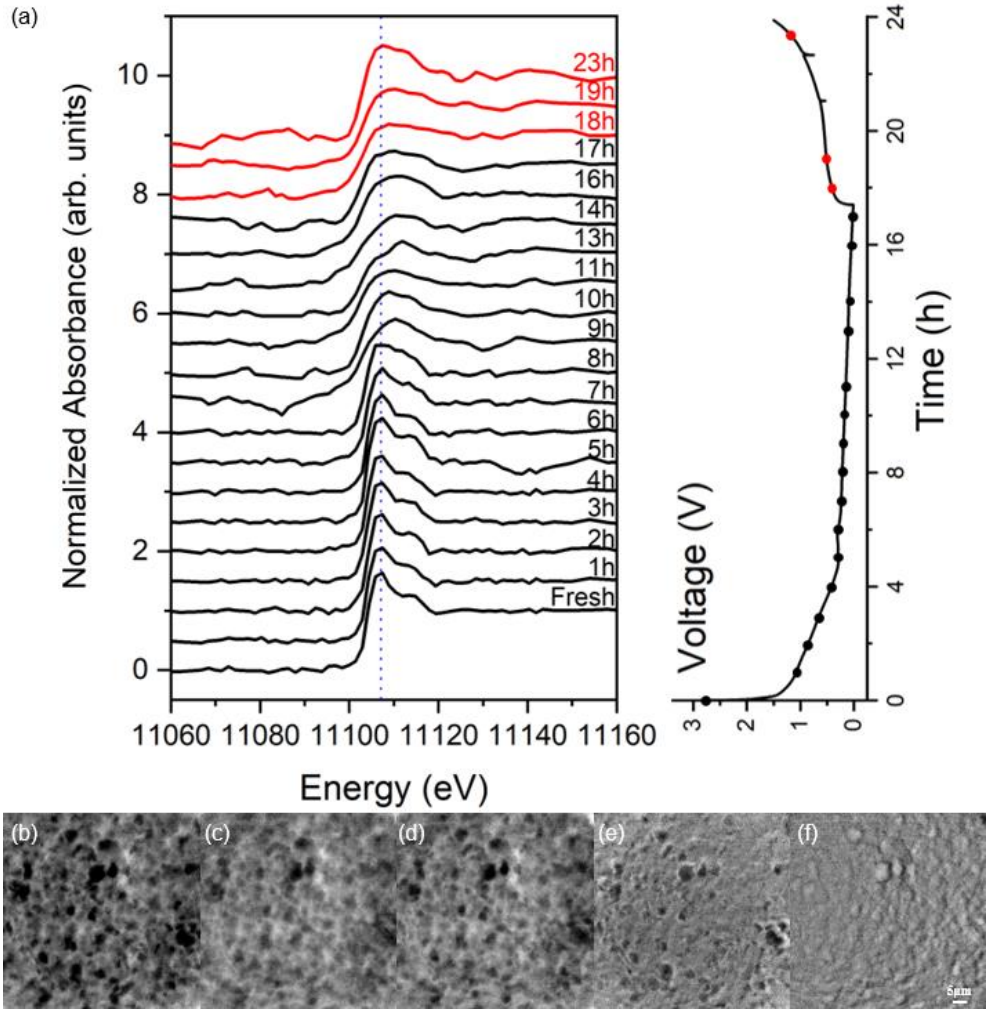

Figure 4. (a) Transmission X-ray microscopy-based germanium XANES spectra and potential plots for $Ge_{0.9}Se_{0.1}$ electrodes cycled at 0.1 C rate. TXM image from (b) pristine, (c)lithiated, (d)delithiated states, and (e) image subtraction between (b) and (c), (f) image subtraction between (c) and (d).

Conclusion

The morphological and phase evolutions of $Ge_{0.9}Se_{0.1}$ anode at the single particle level were investigated via operando TXM, in situ TXM with energy scans and X-ray computed nanotomography for the first time. The results from the in situ single particle cell demonstrate the good reversibility of micron-sized $Ge_{0.9}Se_{0.1}$ particles at a 1 C rate. The same $Ge_{0.9}Se_{0.1}$ material at the coin cell scale was tested for comparison as well. The traditional coin cells with complex architectures lead to interactions between each component, therefore, limiting the understanding of the dynamic properties of the active material, especially at high rates. The X-ray-induced damage on polymer binders makes the operando experiment even more difficult. This in situ single particle cell will assist in understanding the dynamic electrochemical processes of electrode materials without the interference of inactive materials in the battery electrode as well as the X-ray-induced damage.

Experimental Section

Fabrication of the in situ single particle cell

The synthesis of $Ge_{0.9}Se_{0.1}$ has been reported previously in ref [10]. The working electrode was fabricated by attaching a $Ge_{0.9}Se_{0.1}$ particle to a precoated tungsten probe via ion beam carbon deposition performed on a Zeiss Nvision 40 FIB-SEM at the Center of Nanoscale Materials, Argonne National Laboratory. The tungsten probe (Ted Pella, Inc. Redding, CA, USA) was coated with polydimethylsiloxanes (PDMS, Sylgard 184, Dow Corning, Auburn, MI, USA) that suppressed the tungsten oxidation side reaction. A thin layer of carbon was deposited where the particle contacts the conductive probe using the sputtering function of the FIB to ensure a stable and low-resistance electrical contact. A small piece of lithium metal (thickness of 0.6 mm foil, Sigma-Aldrich, St. Louis, MO, USA) was attached to a copper wire (Alfa Aesar, Reston, VA, USA) as a counter electrode. Both electrodes were placed inside a quartz capillary tube (Hampton, Aliso Viejo, CA, USA) with a diameter of 3 mm. The wall thickness is 10 μm where the particle is located. 1M $LiPF_6$ electrolyte in a 1:1 volume ratio mixture of ethylene carbonate and dimethyl carbonate solution (Sigma-Aldrich, St. Louis, MO, USA) was injected into the capillary tube via a micro-syringe. The open end of the quartz capillary housing was sealed via 5 min epoxy followed by torr epoxy (Torr seal vacuum epoxy, Agilent Technologies, Lexington, MA, USA) to prevent leaking of the electrolyte. The entire in situ cell assembly was performed in an argon-filled glovebox (under O_2<0.1 ppm, H_2O<0.5 ppm, Unilab 2000, Mbraun, Stratham, NH, USA). The $Ge_{0.9}Se_{0.1}$ cell was cycled at a constant current (approximately 1 C) controlled by a Keithley 6430 subfemtoamp sourcemeter (Tektronix, Beaverton, OR, USA). The in situ cell assembly is depicted in Figure 5.

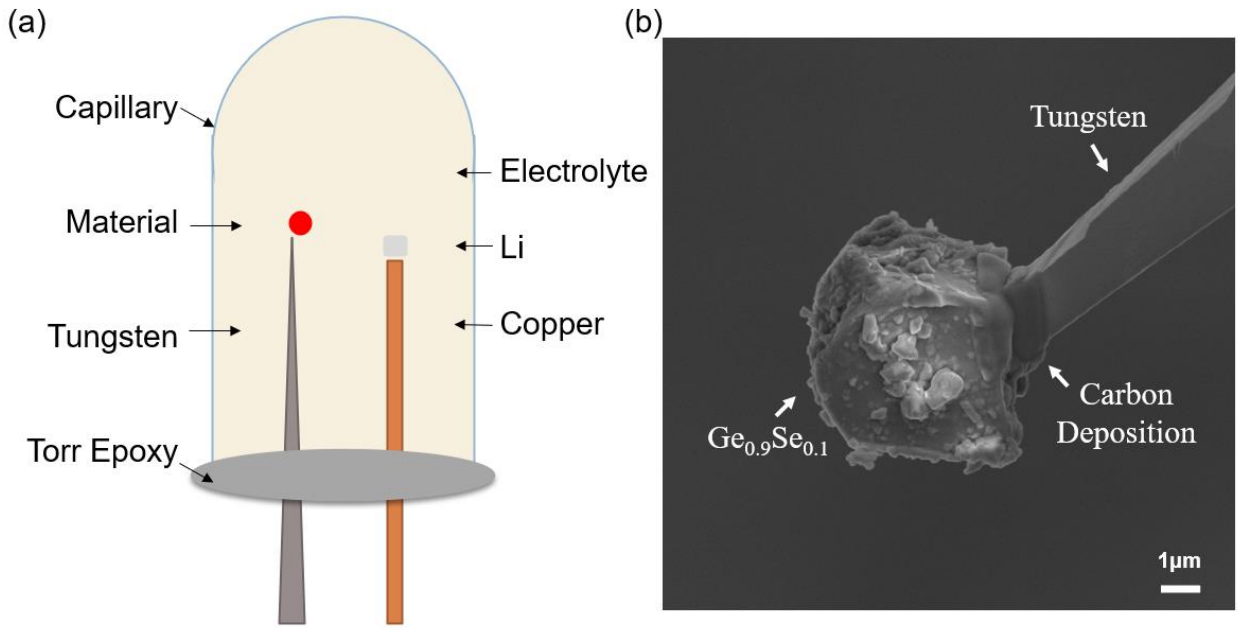

Figure 5. (a) Schematic of the single particle cell assembly. (b) An SEM image of a $Ge_{0.9}Se_{0.1}$ particle attached to a tungsten probe by carbon deposition.

In situ coin cell assembly

The $Ge_{0.9}Se_{0.1}$ electrode for XANES was fabricated from a 50:30:20 (weight%) mixture of active material, carbon black, and polyvinylidene difluoride (PVDF). The mixture was added into the NMP solution and mixed homogeneously for 12 h. The produced slurries were coated onto a thin copper foil and dried at 100 °C in a vacuum oven for 12 h. Circular discs with a 1.11 cm diameter were punched out of the electrode films and stored in an argon-filled glove box for coin cell assembly. Traditional CR2032 coin cells were modified and used in this study. 2 mm diameter holes were punched at the center of both anode and cathode cases and sealed with 30 μm thick Kapton tape on both sides of the case. Figure 6 displays the order of the operando coin cell assembly. The stainless-steel current collector on top of the anode case with a 2 mm hole

was to maximize the contact of the electrode. The electrode was placed on the collector followed by adding 20 µL $LiPF_6$ electrolyte. A Celgard 2400 separator was placed on top of the electrode with an additional 20 µL electrolyte placed on top of it. A piece of lithium metal with a 1.27 mm diameter was laid on the separator followed by another stainless-steel plate (with a 2 mm hole at the center) and wave spring. The cell was crimped and taken out of the glove box for electrochemical evaluation.

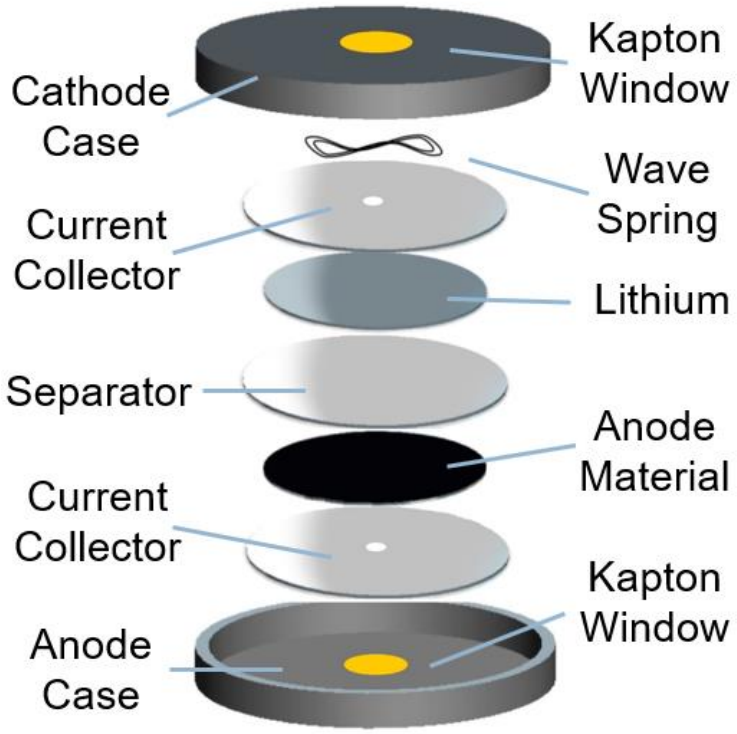

Figure 6. In situ coin cell assembly.

Operando transmission X-ray microscopy and in situ tomography measurements

Transmission X-ray microscopy has been increasingly used in the field of battery research during the past few years. The operando synchrotron-based TXM with a field of view of 94 µm by 78

μm at 38.4 nm pixel size was implemented periodically to capture the morphological information in real-time for the $Ge_{0.9}Se_{0.1}$ cell. The experiment was conducted at beamline 32-ID-C at the Advanced Photon Source of the Argonne National Laboratory equipped with a Si 111 double crystal monochromator which enables an energy resolution of $\triangle E/E = 10^{-4}$. Two-dimensional operando TXM images were consecutively collected to monitor the single particle under operating conditions. We employed a 2.5 min time interval between data acquisition with an exposure time of 1 s. A schematic of the TXM is depicted in Figure 7. The X-ray beam is focused down to micrometers by the condenser. The beam stop and pinhole are used to block unfocused X-ray beams. The transmitted photons can illuminate the sample, thereafter, generating magnified images by the Fresnel zone plate and collected by the detector. In order to perform 3D visualization and quantification analysis, we captured a series of 361 images over a 180° rotation with an exposure time of 1s and step size of 0.5° to generate a computed tomographic dataset.

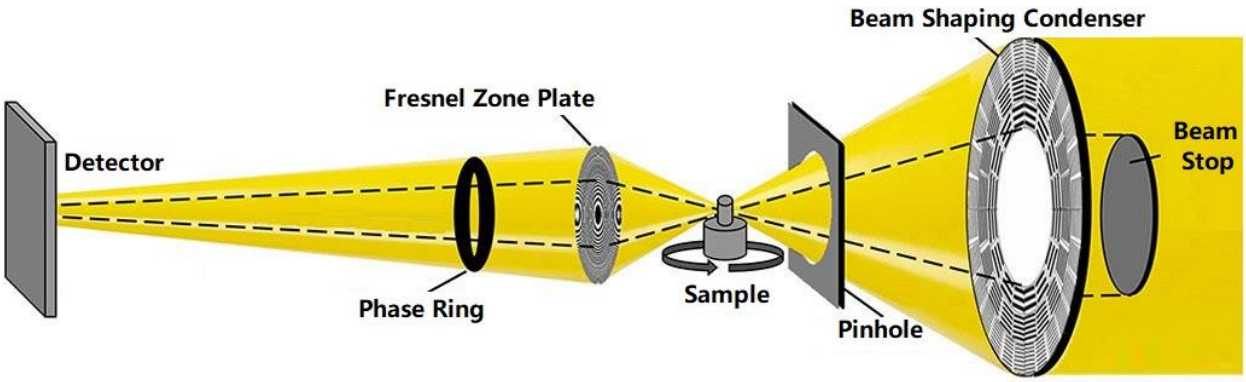

Figure 7. Schematic of the synchrotron-based transmission X-ray microscopy setup [13].

Transmission X-ray microscopy with energy scan

The absorption contrast is the most common TXM imaging mode for material research based on X-ray attenuation changes through a sample being imaged. The Beer-Lambert Law relates the X-ray absorption to the composition and thickness of the sample through which the beam is traveling. X-ray absorption occurs when the photon energy approaches a defined energy shell of a specific element. The energy values applied and their corresponding spectrum imaged could be utilized as an indicator of the chemical composition and its oxidation status. To obtain spectroscopy imaging, a set of images at different energies from 11050 to 11200 eV across the K-edge of germanium were collected. Different step sizes were adopted with 5 eV for pre-edge before 11075 eV, 4eV for post-edge after 11150 eV, and 1.5 eV between 11075 to 11150 eV for the Ge XANES range. Flat and dark images were collected for normalization followed by a 2 × 2 × 2 three dimensional median filter.

Image processing

The series of nanotomography images were reconstructed using Tomopy [14] with a combination of simultaneous iterative reconstruction techniques via the ASTRA Toolbox [15]. A 3D Median filter was employed for both the reconstructed and XANES images via the commercial software Avizo® to remove random noise caused by sharp and sudden disturbances in the image signal. Image registration which is the process of aligning all the images into the same coordinates based on the gravitational center and intensity gradient of each image was conducted after the noise removal. The result images were subject to further analysis. OD analysis was performed in the same manner as in ref [8].

Acknowledgments

This work was supported by US National Science Foundation under Grants No. 1603847 and No. 1603491. CBM gratefully acknowledges support from the Robert A. Welch foundation through grant F-1436. We also used resources related to the Advanced Photon Source, a U.S. Department of Energy (DOE) Office of Science User Facility operated for the DOE Office of Science by Argonne National Laboratory under Contract No. DE-AC02-06CH11357.

Conflict of Interest

The authors declare no conflict of interest.

References

[1] P.-C. Tsai, B. Wen, M. Wolfman, M.-J. Choe, M. S. Pan, L. Su, K. Thornton, J. Cabana, Y.-M. Chiang, *Energy & Environmental Science* **2018**, *11*, 860-871.

[2] S.-M. Bak, Z. Shadike, R. Lin, X. Yu, X.-Q. Yang, *NPG Asia Materials* **2018**, *10*, 563-580.

[3] T. Li, X. Zhou, Y. Cui, C. Lim, H. Kang, B. Yan, J. Wang, J. Wang, Y. Fu, L. Zhu, *Electrochimica Acta* **2019**, *314*, 212-218.

[4] a) L. Y. Lim, N. Liu, Y. Cui, M. F. Toney, *Chemistry of Materials* **2014**, *26*, 3739-3746; b) K. E. Silberstein, M. A. Lowe, B. Richards, J. Gao, T. Hanrath, H. D. Abruña, *Langmuir* **2015**, *31*, 2028-2035.

[5] O. J. Borkiewicz, B. Shyam, K. M. Wiaderek, C. Kurtz, P. J. Chupas, K. W. Chapman, *Journal of Applied Crystallography* **2012**, *45*, 1261-1269.

[6] C. Lim, H. Kang, V. De Andrade, F. De Carlo, L. Zhu., *J. Synchrotron Radiat.* **2017**, 24, 695-698.

[7] a) J. Wang, K. Chen‐Wiegart Yu‐chen, J. Wang, *Angewandte Chemie International Edition* **2014**, *53*, 4460-4464; b) J. Wang, C. Eng, Y.-c. K. Chen-Wiegart, J. Wang, *Nature Communications* **2015**, *6*, 7496.

[8] T. Li et al., *Journal of Materials Chemistry A* **2019**. see Supporting Information.

[9] a) X. Zhou, T. Li, Y. Cui, Y. Fu, Y. Liu, L. Zhu, *ACS Applied Materials & Interfaces* **2019**, *11*, 1733-1738; b) X. Zhou, T. Li, Y. Cui, M. L. Meyerson, C. B. Mullins, Y. Liu, L. Zhu, *ACS Applied Energy Materials* **2019**; c) X. W. Zhou, T. Y. Li, Y. Cui, M. L. Meyerson, J. A. Weeks, C. B. Mullins, Y. Jin, Y. Z. Liu, L. K. Zhu, *Acs Applied Energy Materials* **2020**, *3*, 6115-6120; d) X. Zhou, T. Li, Y. Cui, M. Meyerson, J. Weeks, C. B. Mullins, Y. Jin, Y. Liu, L. Zhu, *Acs Applied Materials & Interfaces* **2020**, *12*, 47574–47579; e) B. Q. Xiong et al., *Advanced Energy Materials* **2020**, *10*; see Supporting Information f) R. Amine et al., *Nano Energy* **2020**, *74*; see Supporting Information g) B. Q. Xiong et al., *ACS Energy Letters* **2020**, *5*, 3490–3497. see Supporting Information.

[10] K. C. Klavetter, J. Pedro de Souza, A. Heller, C. B. Mullins, *Journal of Materials Chemistry A* **2015**, *3*, 5829-5834.

[11] F. Wang, L. Wu, B. Key, X.-Q. Yang, C. P. Grey, Y. Zhu, J. Graetz, *Advanced Energy Materials* **2013**, *3*, 1324-1331.

[12] G. Bunker, in *EXAFS and Near Edge Structure III* (Eds.: K. O. Hodgson, B. Hedman, J. E. Penner-Hahn), Springer Berlin Heidelberg, Berlin, Heidelberg, **1984**, pp. 268-272.

[13] V. De Andrade, A. Deriy, M. J. Wojcik, D. Gürsoy, D. Shu, K. Fezzaa, F. De Carlo, *SPIE Newsroom* **2016**.

[14] D. a. Gürsoy, F. De Carlo, X. Xiao, C. Jacobsen, *J Synchrotron Radiat* **2014**, *21*, 1188-1193.

[15] W. van Aarle, W. J. Palenstijn, J. Cant, E. Janssens, F. Bleichrodt, A. Dabravolski, J. De Beenhouwer, K. Joost Batenburg, J. Sijbers, *Opt. Express* **2016**, *24*, 25129-25147.

Supporting Information

T. Li, C. Lim, Y. Cui, X. Zhou, H. Kang, B. Yan, M. L. Meyerson, J. Weeks, Q. Liu, F. Guo, R. Kou, Y. Liu, V. De Andrade, F. De Carlo, Y. Ren, C. Sun, C. Mullins, L. Chen, Y. Fu, L. Zhu, *Journal of Materials Chemistry A* **2019**.

B. Q. Xiong, X. W. Zhou, G. L. Xu, Y. Z. Liu, L. K. Zhu, Y. C. Hu, S. Y. Shen, Y. H. Hong, S. C. Wan, X. C. Liu, X. Liu, S. L. Chen, L. Huang, S. G. Sun, K. Amine, F. S. Ke, *Advanced Energy Materials* **2020**, *10*

R. Amine, A. Daali, X. W. Zhou, X. Liu, Y. Z. Liu, Y. Ren, X. Y. Zhang, L. K. Zhu, S. Al-Hallaj, Z. H. Chen, G. L. Xu, K. Amine, *Nano Energy* **2020**, 74.

B. Q. Xiong, X. Zhou, G. L. Xu, X. Liu, Y. Hu, Y. Liu, L. Zhu, C.-G. Shi, Y.-H. Hong, S.-C. Wan, C.-J. Sun, S. Chen, L. Huang, S.-G. Sun, K. Amine, F.-S. Ke, *ACS Energy Letters* **2020**, *5*, 3490–3497.

Captions for Figures and Schemes

Figure 1. The TXM and corresponding 3D morphological evolutions of a single $Ge_{0.9}Se_{0.1}$ particle cell at the (a,d) pristine, (b,e) lithiated, and (c,f) delithiated states. (g) XANES spectra generated via transmission X-ray microscopy images.

Figure 2. (a, c) Area of interest as highlighted in yellow of the single $Ge_{0.9}Se_{0.1}$ particle cell and (b, d) the corresponding optical density and line profile analysis results at the selected time frame. The cell was under relaxation with no current between 1.6-2.1 h during imaging for in situ tomography and XANES.

Figure 3. (a) Potential plots of a $Ge_{0.9}Se_{0.1}$ electrode cycled at a 1 C rate in the in situ coin cell and (b) the corresponding transmission X-ray microscopy-based germanium XANES spectra. (c) TXM image of the pristine $Ge_{0.9}Se_{0.1}$ electrode. (d) TXM image of the lithiated $Ge_{0.9}Se_{0.1}$ electrode. (e) TXM image of the delithiated $Ge_{0.9}Se_{0.1}$ electrode. (f) differences between (c) and (d) by image subtraction. (g) differences between (d) and (e) by image subtraction.

Figure 4. (a) Transmission X-ray microscopy-based germanium XANES spectra and potential plots for $Ge_{0.9}Se_{0.1}$ electrodes cycled at 0.1 C rate. TXM image from (b) pristine, (c)lithiated, (d)delithiated states, and (e) image subtraction between (b) and (c), (f) image subtraction between (c) and (d).

Figure 5. (a) Schematic of the single particle cell assembly. (b) An SEM image of a $Ge_{0.9}Se_{0.1}$ particle attached to a tungsten probe by carbon deposition.

Figure 6. In situ coin cell assembly.

Figure 7. Schematic of the synchrotron-based transmission X-ray microscopy setup [13].